INTERNATIONAL JOURNAL FOR NUMERICAL METHODS IN FLUIDS, VOL. 3, 507–526 (1983)

WAVE ENVELOPE AND INFINITE ELEMENTS FOR ACOUSTICAL RADIATION*

R. J. ASTLEY

Department of Mechanical Engineering, University of Canterbury, Christchurch, New Zealand

SUMMARY

Finite element models are presented for the calculation of near and far field acoustical radiation. These models are applied to the specific problem of fan noise radiation from axisymmetric turbofan inlets. In all cases conventional acoustic finite elements are used within an inner region close to the inlet. The far field is represented by infinite elements or wave envelope elements. Theory and results are presented for the case with zero mean flow. Comparisons of computed data with analytic solutions and measured values establish the utility of both the infinite element and wave envelope element schemes in determining the near field values of acoustical pressure. The wave envelope scheme is shown to be effective also in the far field. Both schemes use meshes an order of magnitude more sparse that would be required in conventional numerical discretizations, and may consequently be applied at modest computational cost.

KEY WORDS Finite Elements Infinite Elements Acoustics Wave Propagation Radiation

1. INTRODUCTION

Finite element (FE) methods have been used extensively in recent years to model linear acoustical fields. Harmonic time dependence may frequently be removed from the problem prior to discretization. A Helmholtz or modified Helmholtz equation then results for the acoustical pressure amplitude or velocity potential. The boundary conditions of such problems typically involve prescribed impedance conditions or structural-acoustical coupling. Such applications have been the subject of several recent review articles[1–3] and will not be discussed here in further detail except to observe that most of the problems investigated to date have involved bounded enclosures. The difficulties of coupling such finite element solutions (or those from any other numerical scheme) to a suitable far field solution incorporating anechoic conditions at large distances from the exciting mechanism, have received less attention to date. It is for problems of this type that the schemes proposed in this paper are presented. The methods proposed are direct numerical schemes and do not involve matching of numerical and analytic solutions to obtain valid far field descriptions. This is a desirable feature for application to problems where the acoustical field is propagating on a non-zero-mean flow. In such cases simple separable far field solutions are seldom available and methods which rely on their existence (e.g. mode matching) are generally

* This invited paper is an extended, and refereed version of one presented at the Fourth International Symposium on Finite Elements in Flow Problems held in Tokyo, Japan, January 26–29, 1982.

0271–2091/83/050507–20$02.00
© 1983 by John Wiley & Sons, Ltd.
Received 7 December 1982
Revised 28 May 1983

inapplicable. Although the methods described in this paper are presented for the case without mean flow it is towards an ultimate application to the case with flow that the work is directed.

The formulations proposed in this paper are developed and tested with reference to a specific physical application, that of fan-noise radiation from the inlet region of turbofan aircraft engines. A brief review of this problem now follows.

1.1. *The turbofan inlet problem*

Much attention has been given in recent years to the development of numerical schemes for the prediction of fan noise in the vicinity of turbofan inlets. Such work has formed part of a broader effort directed towards the reduction of noise generated by commercial turbofan aircraft. Methods for predicting the modification of the acoustical field as it passes through the ducted (and usually acoustically treated) sections of turbofan inlets are well advanced and include wave envelope weighted residual schemes,[4] FE schemes of various types,[5,6] and transient finite difference schemes,[7,8] all of which seem capable of handling the linear problem for realistic frequencies and Mach numbers.

The propagation of sound in the external region, which extends from the throat of the inlet to the far field, presents a more demanding computational problem since it requires the imposition of radiation type boundary conditions at an infinite (or at least distant) boundary. None of the numerical schemes currently developed for the ducted sections of the inlet may be conventionally applied to the exterior region, since the dimensionality of the linear matrix problem then required to resolve the relatively short wavelength disturbances typical of real inlets is prohibitively large.

A more subtle approach is therefore required and a means must be found of confining the purely numerical portion of the solution within a relatively small computational domain close to the inlet itself. One such approach involves the application of boundary integral methods to the outer region, effectively modelling the outer field by a distribution of source functions over a control surface enclosing the inlet.[9] The impedance on this surface may then be matched iteratively to that of a conventional FE numerical solution in the inner region. This method has produced promising results although it currently appears to present practical difficulties when strongly cut-on modes are present in the inlet.[9]

An alternative approach pursued by the present author[10,11] and further developed in the current paper involves the modification of the shape and weighting functions within a standard Galerkin FE scheme to accommodate the fine harmonic detail of the solution in the outer region. This is done either through the use of infinite elements—which impose an exaggerated exponential decay on the outer solution and consequently may only safely be used to predict the *effect* of the far field on the near field solution—or by the use of wave envelope elements which incorporate the gross features both of the asymptotic decay and of the harmonic variation within a large but finite outer domain. The wave envelope elements, which conceptually resemble those used for internal duct problems,[10] have the advantage of directly predicting acoustical pressures in the far field.

Infinite element and wave envelope radiation theory is presented in this paper for the case with no mean flow. Some preliminary results are also presented for a simple test case with uniform mean flow. The results which are presented demonstrate the accuracy of the various formulations by comparison with exact solutions for hyperboloid ducts and with experimental measurements for more realistic inlet geometries.

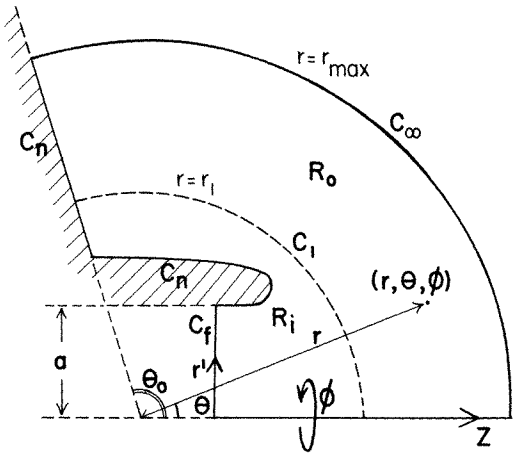

Figure 1. Geometry of the inlet region

2. THEORY

2.1. *Geometry and governing equations*

The geometry of an idealized turbofan inlet is shown in Figure 1. C_n denotes a rigid boundary and is formed, for the purposes of the present analysis, by the surface of the inlet lip and a notional conical surface swept back at an angle θ_0 to the z-axis (if $\theta_0 = 180°$ this surface becomes the centreline behind the inlet). C_f denotes a convenient plane within the inlet at which it is assumed that a known ensemble of incident (i.e. travelling from left to right in Figure 1) acoustical modes is present. C_f will be termed the 'fan plane', although for cases where a uniform segment extends from the actual fan plane to the start of the expanding lip C_f is conveniently moved forward to this point for reasons of computational economy. The region in which a solution will be sought is subdivided into inner and outer subregions R_i and R_o with an interface at the boundary C_1 and an overall outer boundary at C_∞ as shown in Figure 1. The flow within this region is assumed to inviscid, adiabatic and irrotational and may be described by a velocity potential $\Phi(\mathbf{x}, t)$ which has a mean component $\bar{\Phi}(\mathbf{x})$ and a fluctuating acoustical component $\Phi^A(\mathbf{x}, t)$. The acoustical component will be assumed to be of the form

$$\Phi^A(\mathbf{x}, t) = f(r', z)\, e^{i\omega t - im\phi} \tag{1}$$

the term $e^{-im\phi}$ accounting for the presence of spinning acoustical modes generated by rotor–stator interaction. The integer m (sometimes denoted m_ϕ) will be termed the spinning or angular mode number. In the analysis which follows it will be assumed that the mean flow component $\bar{\Phi}(\mathbf{x})$ is zero. The equation governing the acoustical velocity potential amplitude is then[5]

$$f_{r'r'} + \frac{1}{r'} f_{r'} + f_{zz} + \left(k^2 - \frac{m^2}{r'^2}\right) f = 0 \tag{2}$$

where r' and z are cylindrical polar co-ordinates as indicated in Figure 1 and $k = \omega/c_0$ (c_0 denotes the ambient sound speed). Although mean flow is excluded in the theory that follows, the methods of solution presented in this paper have been developed very much with

the inclusion of flow effects in mind. It is therefore worth observing at this stage that if mean flow is included equation (2) is modified by the inclusion of convective mean flow terms and becomes[6]

$$A_1 f_{r'r'} + A_2 f_{zz} + A_3 f_{r'z} + A_4 f_{r'} + A_5 f_z + A_6 f = 0 \tag{3}$$

where the coefficients A_i $(i = 1, \ldots, 6)$ are functions of position and of the mean flow potential.

2.2. *Boundary conditions*

The boundary condition on all rigid surfaces is that of zero normal particle velocity giving

$$\frac{\partial f}{\partial n} = 0 \quad \text{on} \quad C_n \tag{4}$$

where n denotes a co-ordinate locally normal to the boundary.

On the fan plane, C_f, the appropriate boundary conditions may be written

$$f = \sum_{i=1}^{\infty} A_i^+ f_i^+(r') + \sum_{i=1}^{\infty} A_i^- f_i^-(r') \tag{5}$$

and

$$f_z = \sum_{i=1}^{\infty} (-\mathrm{i} k_i^+ A_i^+ f_i^+(r')) + \sum_{i=1}^{\infty} (-\mathrm{i} k_i^- A_i^- f_i^-(r')) \tag{6}$$

where the functions $f_i^{\pm}$ are solutions of the eigenvalue problem in the cylindrical duct section and represent incident and reflected waves propagating with axial wavenumbers $k_i^{\pm}$ (if $k_i^{\pm}$ is real the mode is 'cut-on' and if complex 'cut-off'). The coefficients A_i^+ are assumed known. The coefficients A_i^- must then be found during the course of the solution. Physically the boundary conditions of equations (5) and (6) represent a matching of pressure and normal velocity between regions to the left and right of the fan plane; it being assumed that to the left of C_f a known set of incident modes is present.

At the outer boundary of the solution region a boundary condition must be applied which simulates an anechoic surface. In the present analysis the outer boundary, denoted by C_∞, is a spherical surface at $r = r_{\max}$ (r, θ and ϕ are spherical polar co-ordinates as indicated in Figure 1). It may therefore be assumed that if $r_{\max}$ is sufficiently large the radiated field will behave *locally* as a plane wave propagating outwards from the origin and normally incident on C_∞. This assumption yields the Sommerfeld condition

$$\frac{\partial f}{\partial r} = -\mathrm{i} k f \quad \text{on} \quad C_\infty \tag{7}$$

and is equivalent to the specification of a 'ρc' impedance in acoustical terminology. A useful physical interpretation of equation (7) and one which facilitates its extension to the case with mean flow is to regard it as a statement that at large distances from the inlet the sound field will behave as if it emanates from a single complex source located at the origin. No boundary conditions are required on the z-axis of geometrical symmetry which appears from Figure 1 to constitute an additional boundary of the solution region. This is not in fact the case since the residual schemes described in the following section involve integration over a volume of revolution which contains the z-axis.

2.3. *The residual scheme*

A general weighted residual scheme is now applied to the field equations and boundary conditions described in the preceding sections. An appropriate choice of the basis and weighting functions will then generate a variety of numerical schemes.

First a trial function $\tilde{f}$ is assumed for the velocity potential amplitude f. The trial function is formed as an expansion of known basis functions ψ_i $(i = 1, \ldots, n)$ and unknown coefficients a_i giving

$$\tilde{f} = \sum_{i=1}^{n} a_i \psi_i \tag{8}$$

Substitution of $\tilde{f}$ into equation (2) yields a residual $\tilde{R}$ where

$$\tilde{R} = \tilde{f}_{r'r'} + \frac{1}{r'}\tilde{f}_{r'} + \tilde{f}_{zz} + (k^2 - m^2/r'^2)\tilde{f} \tag{9}$$

The residual is then weighted by an appropriate set of weighting functions W_j $(j = 1, \ldots, n)$ and integrated over the volume of revolution generated by the region bounded by C_f, C_n and C_∞. Integration by parts of the second order terms in equation (9) yields a set of integral equations of the form

$$\int_{R_i+R_o} [-W_{j,r'}\tilde{f}_{r'} - W_{j_z}\tilde{f}_z + (k^2 - m^2/r'^2)W_j\tilde{f}]r'\,dr'\,dz + \int_{C_n} r'W_j\frac{\partial\tilde{f}}{\partial n}\,dS + \int_{C_\infty} r'W_j\frac{\partial\tilde{f}}{\partial r}\,dS - \int_{C_f} r'W_j\frac{\partial\tilde{f}}{\partial z}\,dr' = 0 \tag{10}$$

If the boundary residuals which result from the substitution of the trial function $\tilde{f}$ into the boundary conditions of equations (4), (6) and (7) are also weighted by W_j and integrated over their respective boundaries of revolution, integrated boundary residual equations result of the form

$$\int_{C_n} r'W_j\frac{\partial\tilde{f}}{\partial n}\,dS = 0 \tag{11}$$

$$\int_{C_f} r'W_j\left[\sum_{i=1}^{\infty}(-ik_i^+A_i^+f_i^+(r') - ik_i^-A_i^-f_i^-(r')) - \frac{\partial\tilde{f}}{\partial z}\right]dr' = 0 \tag{12}$$

and

$$\int_{C_\infty} r'W_j\left[\frac{\partial\tilde{f}}{\partial r'} + ik\tilde{f}\right]dS = 0 \tag{13}$$

A linear combination of equations (10), (11), (12) and (13)—obtained by subtracting equations (11), (12) and (13) from equation (10)—then yields a mixed set of weighted field and boundary residual equations of the form

$$\int_{R_i+R_o} (-W_{j,r'}\tilde{f}_{r'} - W_{j_z}\tilde{f}_z + (k^2 - m^2/r'^2)W_j\tilde{f})r'\,dr'\,dz - \int_{C_\infty} r'ikW_j\tilde{f}_j\,dS + \int_{C_f} r'W_j\left[\sum_{i=1}^{\infty}(ik_i^+A_i^+f_i^+(r') + ik_i^-A_i^-f_i^-(r'))\right]dr' = 0 \tag{14}$$

The substitution of equation (8) for $\tilde{f}$ and the truncation of the eigenexpansion of C_f after m terms reduces equations (14) to an incomplete set of linear equations for the coefficients A_i^- and a_i. In matrix form these equations may be written

$$\underset{n\times m}{[\mathbf{B}^-]}\ \underset{m\times l}{\{\mathbf{A}^-\}} + \underset{n\times n}{[\mathbf{C}]}\ \underset{n\times l}{\{\mathbf{a}\}} = -\underset{n\times m}{[\mathbf{B}^+]}\ \underset{m\times l}{\{\mathbf{A}^+\}} \tag{15}$$

where $\{\mathbf{A}^-\}$, $\{\mathbf{A}^+\}$ and $\{\mathbf{a}\}$ are column vectors of the coefficients A_i^-, A_i^+ and a_i, respectively and where the matrices $[\mathbf{B}^-]$, $[\mathbf{B}^+]$ and $[\mathbf{C}]$ are given by

$$B_{ji}^{\pm} = \int_{C_f} r' W_j(\mathrm{i}k_i^{\pm} f_i^{\pm}(r'))\, \mathrm{d}r' \tag{16}$$

and

$$C_{ji} = \int_{R_i+R_o} [-W_{j,r'}\psi_{i,r'} - W_{j,z}\psi_{i,z} + (k^2 - m^2/r'^2) W_j\psi_i] r'\, \mathrm{d}r'\, \mathrm{d}z - \int_{C_\infty} \mathrm{i}kW_j\psi_i r'\, \mathrm{d}S \tag{17}$$

Although equations (15) are incomplete the boundary condition of pressure continuity at C_f (equation (5)) has not yet been incorporated into the residual scheme. This is now done by weighting the residual from equation (5) with a class of weighting functions $W_j' = \mathrm{i}k_j^- f_j^-(r')$, $(j = 1, \ldots, m)$, and integrating over the C_f surface of revolution. An additional set of weighted equations results of the form

$$\underset{m\times m}{[\mathbf{D}^-]}\ \underset{m\times l}{\{\mathbf{A}^-\}} + \underset{m\times n}{[\mathbf{B}^-]^{\mathrm{T}}}\ \underset{n\times l}{\{\mathbf{a}\}} = -\underset{m\times m}{[\mathbf{D}^+]}\ \underset{m\times l}{\{\mathbf{A}^+\}} \tag{18}$$

where $[\mathbf{B}^-]$ is as previously defined and the matrices $[\mathbf{D}^{\pm}]$ are given by

$$D_{ij}^{\pm} = -\int_{C_f} \mathrm{i}k_i^- f_i^-(r') f_j^{\pm}(r') r'\, \mathrm{d}r' \tag{19}$$

For a hard-walled section at C_f the eigenfunctions $f_i^{\pm}(r')$ are orthogonal, yielding diagonal matrices for $[\mathbf{D}^+]$ and $[\mathbf{D}^-]$. Equations (15) and (18) now combine to give a complete set of linear equations in $\{\mathbf{a}\}$ and $\{\mathbf{A}^-\}$. In matrix form this final statement of the discretised problem may be written

$$\begin{bmatrix} \mathbf{D}^- & \mathbf{B}^{-\mathrm{T}} \\ \mathbf{B}^- & \mathbf{C} \end{bmatrix} \begin{Bmatrix} \mathbf{A}^- \\ \mathbf{a} \end{Bmatrix} = -\begin{bmatrix} \mathbf{D}^+ \\ \mathbf{B}^+ \end{bmatrix} \{\mathbf{A}^+\} \tag{20}$$

The above formulation is still general in the sense that it leaves open the choice both of the basis functions ψ_i and of the weighting functions W_j. Some particular choices of these functions are discussed in the following section.

2.4. *Choice of basis and weighting functions*

The residual scheme described in the previous section was implemented with three different sets of basis and weighting functions. The most straightforward of the schemes involves the subdivision of both the inner and outer regions (R_i and R_o) into conventional finite elements. Nine noded isoparametric rectangles were used. A typical element is shown in Figure 2(a). The basis functions ψ_i are then defined by the global shape functions, $N_i(r', z)$, associated with node i of the discretization. The global shape functions are themselves explicitly defined within each element by appropriate element shape functions. The coefficients a_i in the trial expansion therefore correspond to nodal values of f. A standard

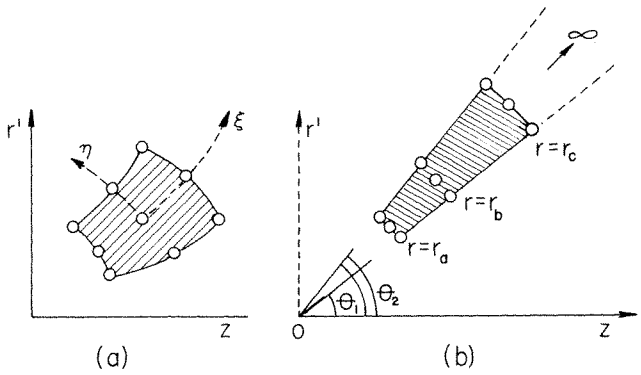

Figure 2. Element topology: (a) a conventional element, (b) an infinite/wave envelope element

Galerkin scheme may then be applied with the basis functions being used also as weighting functions. The contributions to the submatrices $[\mathbf{B}^{\pm}]$ and $[\mathbf{C}]$ of equation (20) are calculated element by element and assembled in the usual way. The uniform duct eigenvectors, $f_i^{\pm}(r')$, and axial wavenumbers, $k_i^{\pm}$, which are required for the evaluation of the integrals in the submatrices $[\mathbf{D}^{\pm}]$ may be determined either analytically or numerically. In all the schemes presented in this paper they were calculated numerically using a compatible FE eigenvalue formulation on the fan plane C_f. This process ensures that the resolution implicit in the eigenfunction expansion of equations (5) and (6) is identical to that of the FE discretization within the adjacent computational region. It also enables the integrals of equation (19) to be evaluated element by element and avoids the necessity of calculating Bessel functions of high order and argument which would occur in the integrands if analytic solutions were used.

The formulation described above will be termed the 'conventional' FE scheme. It has several serious drawbacks when applied to the turbofan inlet problem. The most important of these is inherent in the choice of shape/basis functions. These are quadratic in the local element co-ordinates ξ and η (see Figure 2(a)). Several elements are therefore required to accurately represent a single wavelength variation of the solution in any direction. For realistic frequencies the typical far field acoustical wavelength may be an order of magnitude smaller than the diameter of the inlet and several orders of magnitude smaller than the overall dimension of the computational domain if the outer boundary is sufficiently distant to justify the assumption of a 'ρc' impedance. The number of degrees of freedom then required for useful analysis becomes prohibitively large. It was in an attempt to overcome this basic problem that the 'infinite element' and 'wave envelope' (WE) schemes were developed. These are now described.

In the infinite element and WE schemes a different choice of weight and basis functions is made in the inner and outer computational regions. In the inner region, R_i, both ψ_i and W_i are chosen as for the conventional scheme, i.e. both are equated to the global element shape functions. In the outer region R_o, however, an attempt is made to include the gross features of the harmonic behaviour of the solution within the basis functions themselves. By this means, the elements in the outer region are required to resolve only the discrepancy between the actual solution and the implied harmonic and amplitude variations incorporated in the discretization. Larger elements may therefore be chosen which extend over many wavelengths and a decrease in the overall dimensionality of the problem is anticipated.

The infinite element scheme, which derives from analogous two dimensional water wave

studies,[8] divides the outer region R_o into a single layer of elements. The outer boundary is moved to infinity and the elements are therefore of infinite extent. In the current analysis nine noded Langrangian elements are used with the assumption that the conventional element shape functions for such an element may be extended within the infinite region enclosed by the broken lines in Figure 2(b). It is convenient (but not essential) to create the mesh of infinite elements so that the sides of the elements are surfaces of constant r and θ (r and θ being spherical polar co-ordinates as shown in Figure 1). The basis and weight functions corresponding to any node i within the outer region are then defined by

$$W_i = \psi_i = N_i(r, \theta)\, e^{-(ik+1/L)(r-r_i)} \tag{21}$$

The function $N_i(r, \theta)$ in the above expression denotes the conventional global shape function. The exponential factor in W_i and ψ_i consists of an outward propagating wave-like factor, of wavenumber k, and an exponential radial decay of length scale L. The factor $(r - r_i)$ in the exponential argument ensures that $\psi_i \equiv 1$ at node i (r_i denotes the polar radial co-ordinate of node i) and hence preserves the significance of the coefficients a_i in equation (8) as nodal values of $\tilde{f}$. The element integrations involved in the evaluation of element contributions to C_{ji} from the outer region are more easily performed if spherical (rather than cylindrical) polar co-ordinates are used for the integrands of equation (17). The transformation is tedious but trivial and results in integrals of the form

$$\int_{\theta_1}^{\theta_2} g(\theta) \int_{r_a}^{\infty} \left\{ \left(\sum_{p=0}^{6} \alpha_p r^p \right) e^{-2(ik+1/L)r} \right\} dr\, d\theta \tag{22}$$

A 21-point numerical integration scheme (3 points in the θ direction, 7 points in the radial direction) is used to evaluate these terms. The scheme is exact in the radial direction.[8] The choice of the length scale L is arbitrary to the extent that any value of L which approximately represents the amplitude decay in the vicinity of C_1 will give a reasonable inner solution.[8,9] It is one of the problems of infinite element solutions, however, that whatever rate of exponential decay is chosen it will inevitably fail to represent the whole of the far field solution, which, for three dimensional problems, is characterized by reciprocal decay. This deficiency is remedied in the WE approach.

The WE scheme is initially similar to the infinite element formulation in that the weight and basis functions are once again identified with the global shape functions within the inner region R_i. The outer region however is subdivided into one or more layers of large but finite elements. It is again convenient to orientate these elements in the r and θ directions. The topology of a typical WE element is indicated by the shaded element of Figure 2(b). C_∞ is retained as a finite outer boundary. The basis functions ψ_i in the outer region are then defined by

$$\psi_i = N_i(r, \theta) \frac{r_i}{r} e^{-ik(r-r_i)} \tag{23}$$

where $N_i(r, \theta)$ denotes the conventional global shape function associated with node i. The basis functions so defined incorporate reciprocal decay and a wave-like variation corresponding to a locally outward travelling wave. They also have the property that $\psi_i \equiv 1$ at node i and the coefficients a_i once more retain their significance as nodal values of $\tilde{f}$. The weight functions for the WE scheme are now chosen to be the complex conjugates of the basis functions, i.e.

$$W_i = N_i(r, \theta) \frac{r_i}{r} e^{+ik(r-r_i)} \tag{24}$$

Since the conventional shape functions are real this only affects the harmonic factor but has the attractive consequence of causing the exponential terms within the integrands of equation (17)—which arise from products of W_j, ψ_i and their derivatives—to cancel identically. Conventional Gauss–Legendre numerical integration may therefore be used even though each element extends over many wavelength variations of W_j and ψ_i. For the current analysis 3 point integration is used in the r and θ directions.

3. RESULTS

Three sets of results will be presented for the case with no flow. Initially the performance of the three numerical schemes (conventional, WE and infinite element) is assessed by a comparison of computed and analytic solutions for spinning mode propagation in an hyperboloid expansion. Comparisons then follow between computed and experimental results for realistic inlet geometries initially at relatively low frequencies and lastly for a high frequency case. All results are presented in terms of modal reflection coefficients (where applicable) and values of the acoustical pressure amplitude, p, or sound pressure level (SPL). The numerically calculated values of p are related to the computed velocity potential by $p = \rho_0 i\omega\bar{f}$. The computed results presented in this section were obtained using a frontal solution to perform the main matrix reduction. Typically 1000–2000 degrees of freedom were required with front sizes in the range 40–120. The presentation of results is concluded by a discussion of the case with mean flow and the inclusion of some results for a test case involving structurally generated acoustical fields in a uniform mean flow.

3.1. *Comparison with analytic results*

A useful analytic test solution incorporating many of the features of real inlets—spinning mode propagation, modal mixing, exit reflections—is to be found in an exact solution[13] for sound propagation through a family of hyperboloid ducts. The geometry for which these solutions hold is shown in Figure 3 and consists of a hyperbolic expansion which develops from a cylindrical section and tends asymptotically to a conical surface of cone angle θ_0. Numerical results were calculated using all three FE schemes for the particular case $\theta_0 = 70°$ and $m_\phi = 8$. The frequency range investigated includes the cut-on frequency of the first two modes in the cylindrical section and corresponds to values of the non-dimensional parameter

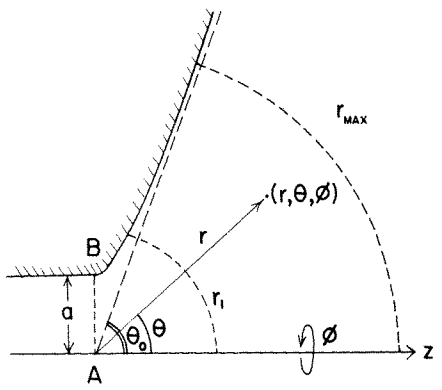

Figure 3. Hyperbolic horn geometry

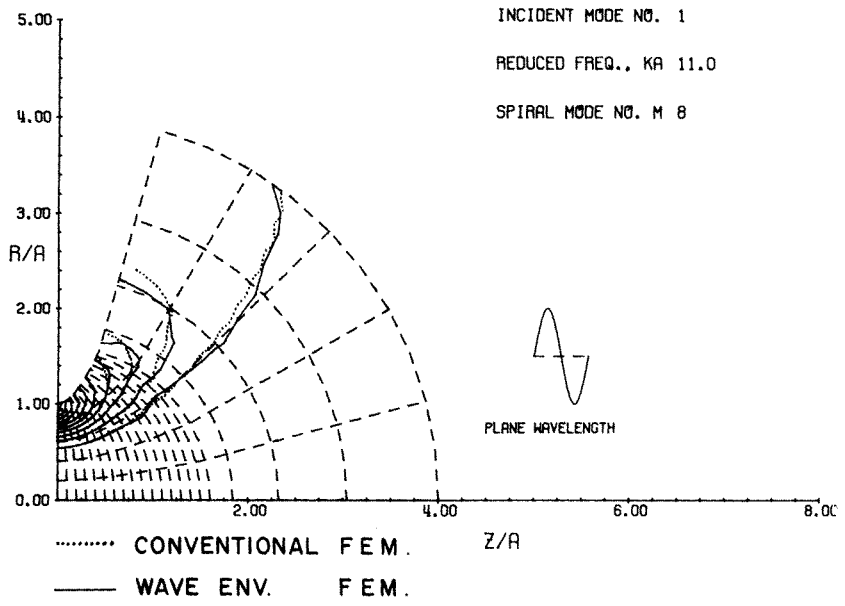

Figure 4. Computed acoustical pressure contours for a hyperbolic duct, ($\theta_0 = 70°$, $ka = 11$, $m_\phi = 8$) conventional and WE solutions

ka in the range $9{\cdot}0 < ka < 15{\cdot}0$. The computed and analytic solutions are presented for single incident modes.

Contour plots of the absolute value of acoustical pressure serve as useful qualitative representations of the numerical solutions. Such plots are shown in Figure 4 for the case $ka = 11$ with mode 1 incident (all other modes being cut off at this frequency). Contours are plotted for the conventional and WE schemes and are superimposed on a representation of the WE mesh which was used to obtain the latter results. The WE mesh for this problem comprised a fine mesh of conventional elements in the region $r < r_1$ ($=1{\cdot}6a$) with four layers of WE elements in the outer region $r_i < r < r_{max}$ ($=4a$). The conventional results plotted were obtained using a mesh with fine resolution over the entire region equivalent to the resolution in the inner region of the WE mesh. Inset in Figure 4 (and in all similar figures to follow) is a representation of the characteristic wavelength of the problem, ($=2\pi/k$). Within the conventional inner region an axial mesh resolution of approximately 5 elements per wavelength is used. Within the WE region this density is decreased to less than one element per wavelength with little perceptible effect on the resulting solution.

Analogous infinite element results are presented in Figure 5(a) which shows pressure contours in the inner region obtained by replacing the WE elements of Figure 4 by a single layer of infinite elements. These contours are in fact in very close agreement with those of Figure 4 within the inner region. They are compared in Figure 5(b) with the equivalent contours obtained by decreasing the dimensionality of the conventional scheme by reducing the value of r_{max} to $1{\cdot}6a$ (equal to r_1 in the WE and infinite element solutions). The solutions of Figures 5(a) and 5(b) therefore represent the same computational effort. It is clear however that the solution of Figure 5(b) contains significant spurious reflections at the C_∞ boundary which is no longer sufficiently distant to justify the 'ρc' impedance. Such effects are not apparent in the infinite element or WE solutions.

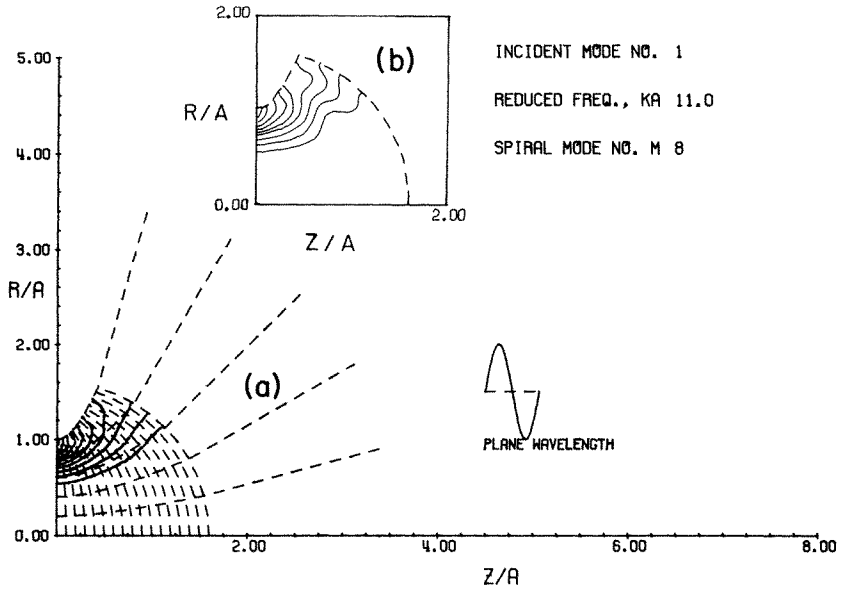

Figure 5. Computed acoustical pressure contours for a hyperbolic duct, ($\theta_0 = 70°$, $ka = 11$, $m_\phi = 8$) infinite element and conventional solutions

The correspondence of all three schemes to the exact solution is demonstrated in Figures 6, 7, and 8. Figures 6 and 7 show analytic and computed values of the reflection coefficients R_{11} and R_{12} at the fan plane—R_{ij} being defined to be the reflection coefficient in mode j with mode i incident—and give a measure of the accuracy of the computed solution in the near field. The absolute value and phase of R_{ij} are plotted against frequency (ka) through cut-on of the first two modes. Figure 8 is a polar plot of computed and exact values for the far field directivity function $f(\theta)$ (defined by $p(r, \theta) \sim f(\theta)/r$ as $r \to \infty$). Values are plotted for modes 1 and 2 incident at a frequency corresponding to $ka = 14{\cdot}5$. Clearly Figures 6, 7, and 8 indicate good agreement between analytic and computed values both in the near and far fields. Discrepancies do appear in Figures 6 and 7 as R_{11} and R_{12} become small. These are partly due to a general loss in accuracy for the reflected portion of the solution as it becomes small compared with the total acoustical field and are also partially attributable to the effects of small spurious reflections at the 'ρc' boundary which become a significant portion of the reflected field if R_{11} or R_{12} is sufficiently small. It is noticeable in this regard that the infinite element scheme is the most accurate of the three formulations in predicting the reflection coefficients. This appears to be a consequence of its implicit removal of the 'ρc' termination—to infinity—and avoidance thereby of any spurious reflections. The infinite element scheme cannot however predict the far field and the far field directivity comparisons of Figure 8 consequently include only conventional, WE and analytic solutions. Of interest in Figure 8 is the effect of varying r_{max} in the conventional scheme. For $r_{max} = 1{\cdot}6a$ the computed directivity function is significantly distorted by near field effects. For the larger value of r_{max} ($=4a$) the conventional and WE schemes are however in excellent agreement with the analytic far field values.

3.2. *Comparison with experiment*

A comparison of WE and experimental results is now presented for two inlet configurations. The first of these is an elliptical 'flight inlet' for which experimental data were obtained

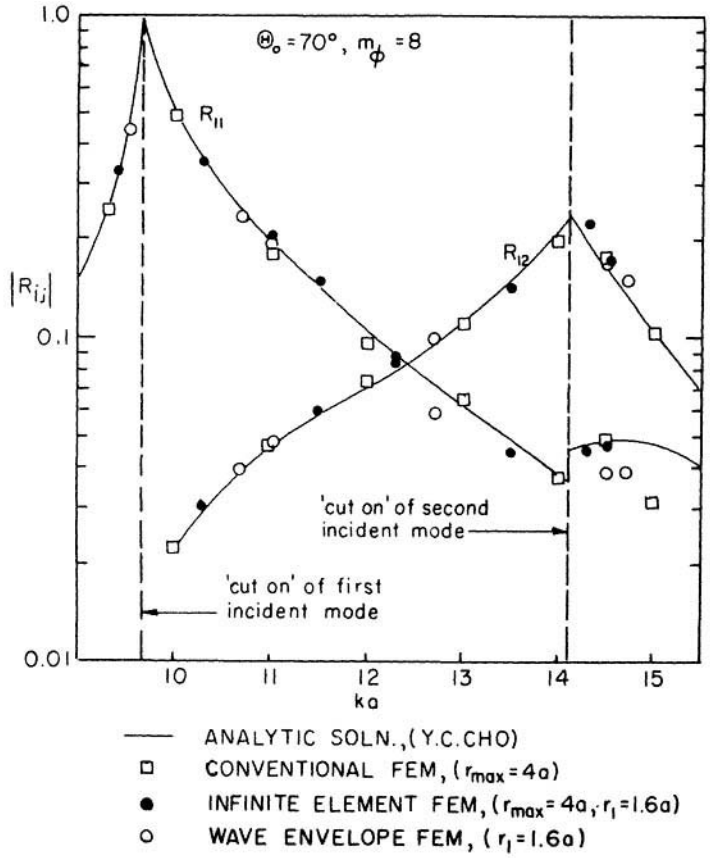

Figure 6. Computed and exact reflection coefficients for a hyperbolic duct ($\theta_0 = 70°$, $m_\phi = 8$), absolute value

in the NASA Langley spinning mode test facility.[14] Although the measured data are for relatively low frequencies and angular mode numbers ($m_\phi = 1$) they are particularly valuable for comparison purposes since they include measurements both of the modal composition at the fan plane and of the far field sound pressure levels. The far field results may therefore be related to known incident mode amplitudes and a comparison made on the basis of the magnitude *and* directivity of the far field SPL. The second test case is for a high frequency inlet for which directivity SPL measurements must be arbitrarily normalized for comparison with the computed solution.

Comparisons of WE results and measured data for the first inlet are presented for two frequencies corresponding to $ka = 2{\cdot}66$ and $ka = 7{\cdot}68$. For the lower of these values the first mode only is cut-on at the throat of the inlet and the measured amplitude of this single progressive mode is used as data for the computed WE solution. In the second case the first and second modes are cut-on and measured values of the amplitude and phase of each mode are used as data for the WE program. Results are presented in the form of computed contour plots of SPL—giving a qualitative description of the computed solution in the near and far field—and comparisons of computed and measured values of the far field SPL directivity.

Computed contours of SPL over the whole computational domain are shown in Figure 9

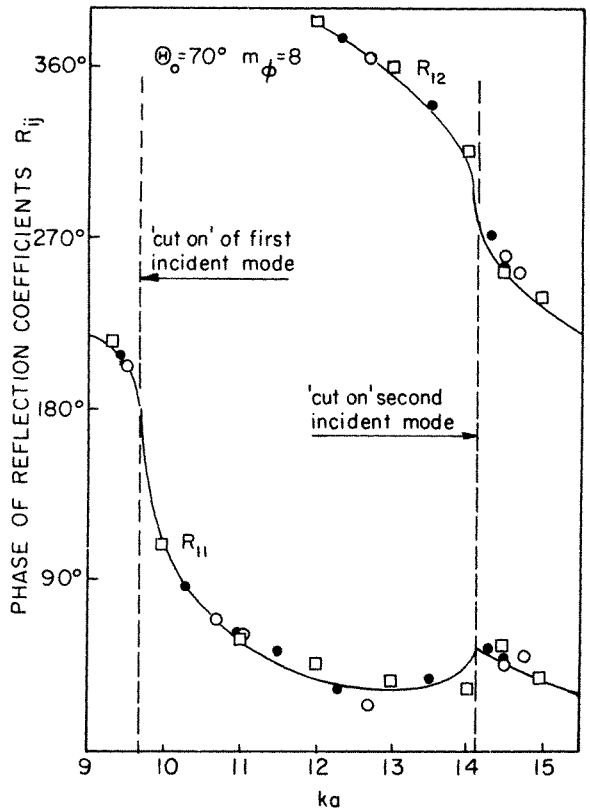

Figure 7. Computed and exact reflection coefficients for a hyperbolic duct ($\theta_0 = 70°$, $m_\Phi = 8$), phase (key as for Figure 6)

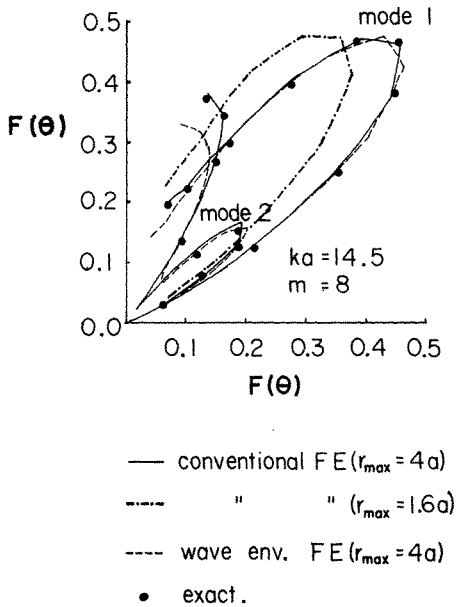

Figure 8. Computed and exact directivity patterns for a hyperbolic duct ($\theta_0 = 70°$, $ka = 14{\cdot}5$, $m_\Phi = 8$)

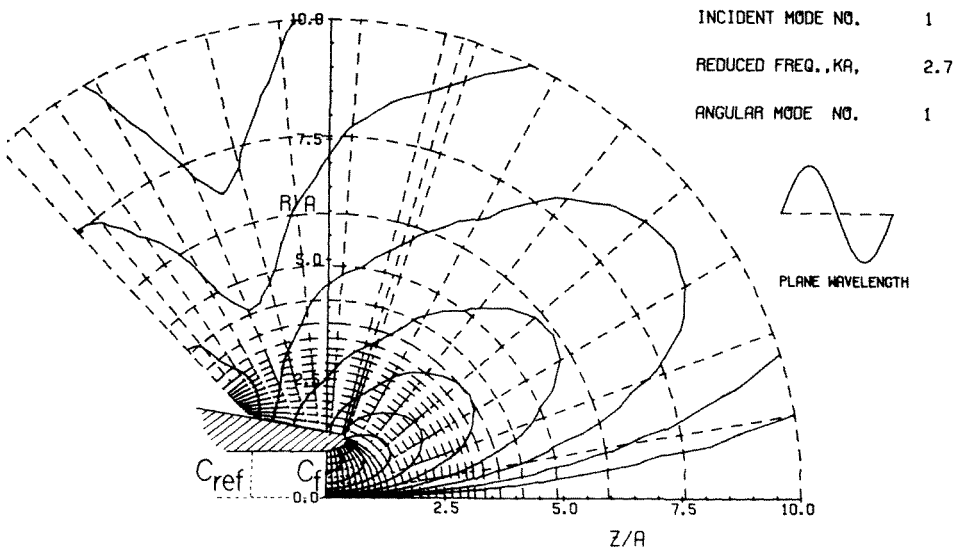

Figure 9. Computed acoustical pressure contours for a flight inlet, ($m_\phi = 1$, $ka = 2{\cdot}66$), WE solution

for $ka = 2{\cdot}66$. They are plotted at 8 dB increments and are superimposed on a representation of the FE mesh. The outer region of the mesh contains 8 layers of WE elements and extends from $r_1 = 3a$ to $r_{max} = 10a$. The inlet lip geometry is indicated by the shaded region near the fan plane C_f. A rear (and fictitious) computational boundary is placed 135° behind the centreline. The corresponding comparison of measured and computed far field SPL values is shown in Figure 10. Two measured curves are shown corresponding to measurements at $\phi = 0°$ and $\phi = 180°$. For this far field comparison, as for all that follow, the computed solution at C_∞ (in this case at $r = 10a$) is assumed to determine the 'asymptotic' far field directivity function $f(\theta)$. This is then used to determine actual pressure levels at specific radii ($r = 20{\cdot}3a$ in this case) where measured data are available. It must be assumed of course that the asymptotic solution holds at the distances involved, an assumption which is easily checked by increasing the value of r_{max} in the computed solution and noting any variation in $f(\theta)$. For this particular case WE solutions were obtained for $r_{max} = 20a$ and

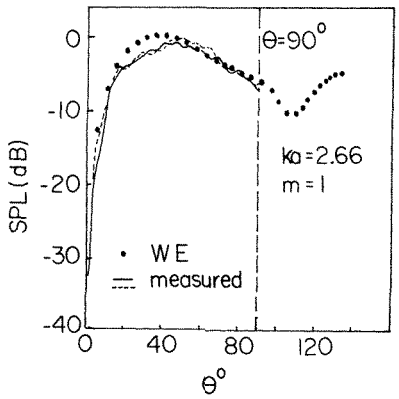

Figure 10. Computed and measured SPL directivity for a flight inlet, ($m_\phi = 1$, $ka = 2{\cdot}66$)

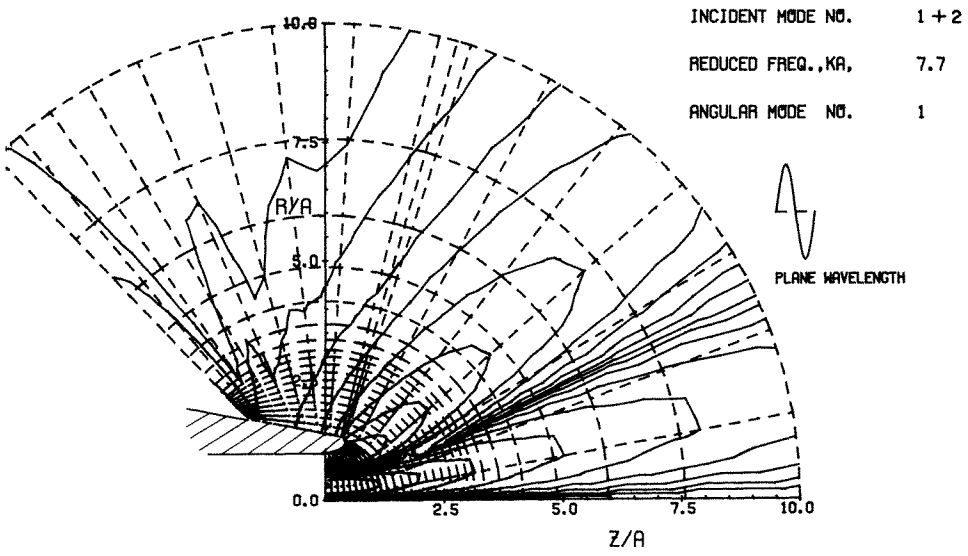

Figure 11. Computed acoustical pressure contours for a flight inlet, ($m_\phi = 1$, $ka = 7{\cdot}68$), WE solution

$r_{max} = 30a$ with little perceptible alteration to the computed SPL values of Figure 10. Since comparisons are being made effectively on the basis of asymptotic behaviour some latitude is also consistently permitted in the choice of the computational origin. In this case the computational origin is at the fan plane C_f, of Figure 9 whereas the experimental origin is at a reference plane C_{ref} also shown. Asymptotically this difference will not affect the far field directivity and no adjustment of data was therefore considered necessary.

From Figure 10 it is clear that excellent agreement exists between the measured and predicted data, certainly in the forward quadrant ($\theta < 90°$). The presence of the rear computational boundary causes some reflection (clearly seen in Figure 9) but does not affect the forward directivity pattern if the boundary is sufficiently oblique to the inlet. In general it has been found—after numerical experimentation with a number of inlets—that provided the computational boundary is approximately 90° to the rear of the principal radiation lobe its effect on forward radiation is sufficiently small to be neglected.

Results for the same inlet at a higher frequency ($ka = 7{\cdot}68$) are presented in the same format in Figures 11 and 12. The relative modal amplitudes of the first and second incident modes are in the ratio of 1:3 respectively with a phase lag at C_{ref} of 42°. The dominance of the second mode causes the pronounced two lobed radiation pattern evident in Figures 11 and 12. Once again the comparison between measured and predicted values of SPL, represented by Figure 12, is excellent. It is worth noting that, although the frequencies involved in the solutions of Figures 9–12 are relatively small, the dimensions of the wave envelope elements employed in the discretizations are many times larger than a single characteristic wavelength. The application of a conventional FE scheme even to these low frequency configurations would in fact be prohibitively expensive in terms of the CPU time required.

Finally, a comparison is presented between theory and experiment for an inlet at a (more or less) realistic frequency and angular mode number. The experimental data for this comparison were obtained from tests conducted at the NASA Lweis vertical lift facility.[9] A

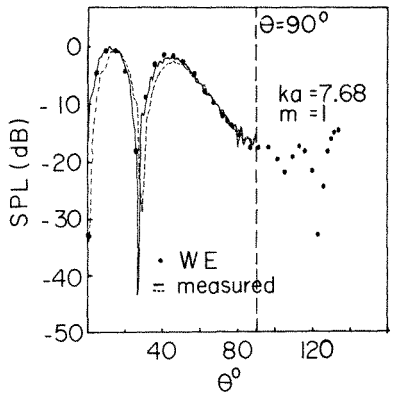

Figure 12. Computed and measured SPL directivity for a flight inlet ($m_\phi = 1$, $ka = 7{\cdot}68$)

JT15D turbofan engine with a rotor–stator arrangement of 41 stator rods and 28 rotor blades was used to produce spinning modes of angular mode number 13. The cut-on frequency for this configuration corresponds to a value of ka in the vicinity of 15·0. The measured data currently available comprise far field SPL measurements normalized to 100 dB at $\theta = 60°$. Data are only available at this time for the case $ka = 15{\cdot}4$, corresponding to a frequency slightly above cut-on of the first mode. All other modes are strongly cut-off. Computed SPL contours (at 8 dB increments) for $ka = 15{\cdot}4$ and $m_\phi = 13$ with mode 1 incident are shown in Figure 13. They are obtained from a WE solution with $r_{max} = 10a$. The mesh used for the calculation of these results is indicated by the broken lines in Figure 13. The far field SPL values predicted by this solution are plotted in Figure 14 and compared with measured values (computed and measured results are both normalized to 100 dB at $\theta = 60°$). Also shown in Figure 14 are WE results for a more extensive mesh with $r_{max} = 30a$

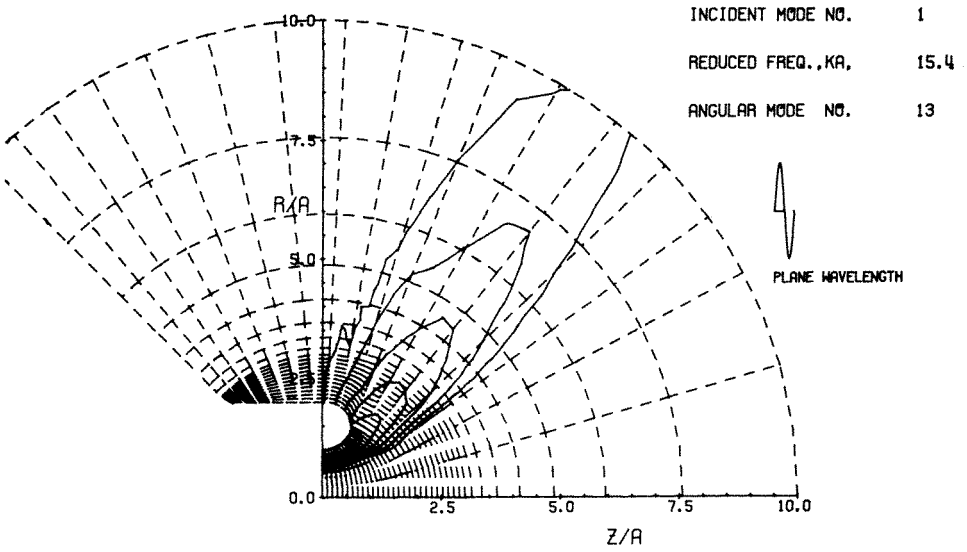

Figure 13. Computed acoustical pressure contours for JT15D inlet, ($m_\phi = 13$, $ka = 15{\cdot}4$), WE solution

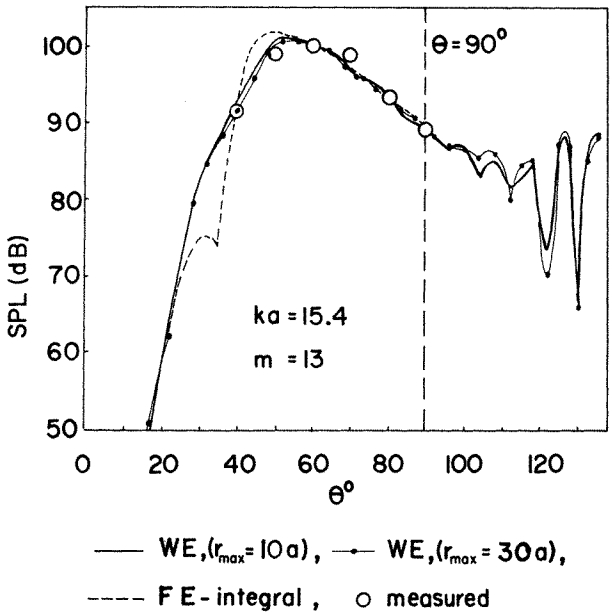

Figure 14. Measured and computed SPL directivity for JT15D inlet ($m_\phi = 13$, $ka = 15{\cdot}4$)

demonstrating a large degree of convergence of the WE far field results to an asymptotic limit as $r_{max}/a \to \infty$. Results from the finite element-integral theory[9] for the same problem are also presented and appear to give somewhat poorer correspondence with the measured values. The measured data is admittedly somewhat sparse but the correspondence between predicted WE results and measured values appears to be good in the forward quadrant. The boundary at $\theta_0 = 134°$ produces spurious reflections which are not well resolved by the numerical solution but which again do not affect the solution greatly in the regions of significant forward radiation.

3.3. *The case with mean flow*

It was noted in Section 2.1 that although the theory presented applies only to the case of a quiescent medium it was developed very much with the inclusion of mean flow effects as the ultimate goal. Details of the modifications required to accommodate such effects lie beyond the scope of the present paper and will be reported in full at a later date. Algebraically the modifications are considerable. Conceptually, however, they involve little that has not already been discussed in the context of the no flow case. The major difference involves the treatment of the far field boundary condition to accommodate convective effects. Ray acoustical theory may be used to accomplish this if the numerical solution is assumed to behave locally at the far field boundary like a wave packet emanating from a source at the origin. For a quiescent medium this assumption is equivalent to the Sommerfeld condition used in the formulation already described. It is convenient to use the ray paths and constant phase surfaces predicted by ray theory as the boundaries of the elements in the outer region. The factor $(1/r)\,e^{-ikr}$ which occurs in the shape function definitions for the no-flow wave envelope elements must then be replaced by a more complicated factor involving the asymptotic behaviour of wave packets travelling along the appropriate ray paths.

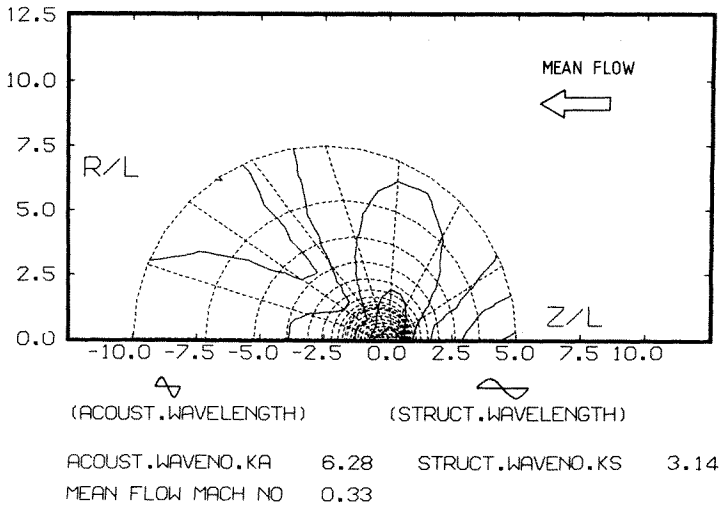

Figure 15. Computed acoustical velocity potential contours for test case with flow ($kL = 6{\cdot}28$, $k_sL = 3{\cdot}14$, $M = 0{\cdot}33$)

The utility of this approach is demonstrated by the inclusion of two figures representing wave envelope solutions for a simple test case with mean flow present. Physically the test case is that of the acoustical field generated by an axially symmetric structural wave of wavenumber k_s travelling along a thin flexible cylinder located near the origin. The cylinder lies along the z-axis and is of finite length L. A uniform flow of Mach number M flows over the cylinder in the negative z direction and is undisturbed if the cylinder is assumed to be of infinitesimal radius. The structural wave is moving in the positive z-direction. An exact far field solution for this problem may be obtained as an integral of volume velocity sources along the z-axis, the strength of the sources being deduced from the effective boundary displacement of the exciting structural wave. Since the mean flow is assumed uniform (i.e. undisturbed by the cylinder) the ray paths and constant phase surfaces due to a source at the origin are straight lines and convected spherical surfaces as indicated by the element boundaries in the sparse outer region of Figure 15. In the same Figure are shown the computed contours of $|\phi|$, at 10 dB increments, calculated using a wave envelope finite element scheme incorporating the effects of mean flow. For this particular solution the frequency parameters were $kL = 2\pi$ and $k_sL = \pi$, with an adverse Mach number $M = 0{\cdot}333$. As with the no-flow results the wavelengths of acoustical and structural waves are also indicated for comparison with the length scales of the solution region and the size of individual elements. A close correspondence between the computed solution represented by the contours of Figure 15 and the exact far field solution mentioned previously is demonstrated in Figure 16 where both solutions are plotted at the outer boundary of the computational region (i.e. the outermost spherical surface indicated by dotted lines in Figure 15). The ordinate of Figure 16 is θ, the polar angle subtended at the origin.

Although the above case with flow is still not entirely representative (since the mean flow is undisturbed by the generating mechanism) it does indicate that the current approach is well able to handle the complications associated with convective effects. Further work on the case with sheared mean flow is now in progress and will be reported at a later date.

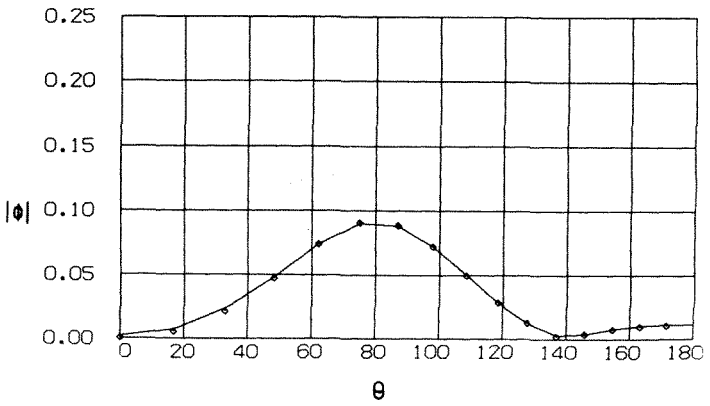

Figure 16. Computed and exact far field velocity potential for test case with flow: ◇ exact,—computed

4. CONCLUSIONS AND GENERAL DISCUSSION

Of the three schemes presented in this paper (conventional, WE and infinite element) it is clear that the latter two are capable of producing useful results for acoustical radiation at relatively high frequencies and angular mode numbers. The conventional scheme is disqualified in this regard by virtue of its inherent dimensionality requirements for short wavelength solutions propogating into the far field. Comparisons with analytic results indicate that both the WE and infinite element schemes are proficient in predicting near field effects and do so at greatly decreased computational cost when compared with the conventional scheme. The WE scheme moreover appears capable of predicting accurate far field behaviour with sparse meshes whose node spacing is large compared with a single wavelength of the resulting solution. It has been shown to give results which are generally in good agreement with experiment.

ACKNOWLEDGEMENTS

The work reported in this paper was performed at the University of Missouri-Rolla and was supported by the NASA Langley Research Center under grant NAG-1-198.

REFERENCES

1. A. Craggs, 'The application of acoustic and absorbtion finite elements to sound fields in small enclosures' in M. M. Kamal ad J. A. Wolf (eds). *Finite Element applications in Acoustics* ASME, 1981, pp. 1–19.
2. D. J. Nefske, J. A. Wolf and L. J. Howell, 'Structural-acoustic finite element analysis of the automobile passenger compartment: a review of current practice', *Journal of Sound and Vibration* 80, 247–266, 1982.
3. W. Eversman and R. J. Astley, 'Further finite element applications: acoustics', in H. Kardestuncer and D. H. Norrie (eds), *Finite Element Handbook* McGraw Hill, New York (in publication).
4. A. H. Nayfeh, B. S. Shaker and J. E. Kaiser 'Transmission of sound through non-uniform circular ducts with compressible mean flow', *AIAA Journal*, **18,** 515–525 (1980).
5. R. K. Sigman, R. K. Majjigi and B. T. Zinn 'Determination of turbofan inlet acoustics using finite elements', *AIAA Journal*, **16,** 1139–1145 (1978).
6. R. J. Astley and W. Eversman, 'Acoustic transmission in lined ducts with flow, Part 2: the finite element method', *Journal of Sound and Vibration*, **74,** 103–121 (1981).
7. K. J. Baumeister, 'Time dependent difference theory for noise propagation in a two-dimensional duct', *AIAA Journal*, **18,** 1470–1476 (1980).
8. A. Cabelli, 'Duct acoustics—a time dependent difference approach for steady state solutions', *Journal of Sound and Vibration*, **85**(4), 423–434 (1982).

9. K. J. Baumeister and S. J. Horowitz, 'Finite element—integral simulation of static and flight fan noise radiation from the JT15D turbofan engine', *NASA Technical Memorandum* 82936, November 1982.
10. R. J. Astley and W. Eversman 'A note on the utility of a wave envelope approach in finite element duct transmission studies', *Journal of Sound and Vibration*, **76,** 595–601 (1981).
11. R. J. Astley and W. Eversman, 'Finite element formulations for acoustical radiation', *Journal of Sound and Vibration*, **88** (1), 47–64 (1983).
12. P. Bettess and O. C. Zienkiewicz, 'Diffraction and refraction of surface waves using finite and infinite elements', *International Journal for Numerical Methods in Engineering*, **11,** 1271–1290 (1977).
13. Y. C. Cho, 'Rigorous solutions for sound radiation from circular ducts with hyperbolic horns or infinite plane baffle', *Journal of Sound and Vibratiom*, **69,** 405–425 (1980).
14. R. J. Silcox, 'Experimental investigation of geometry and flow effects on acoustic radiation from duct inlets', *AIAA Paper*, 83–0713, 8th Aeroacoustics Conference, Atlanta, Georgia, 1983.